PROCEEDINGS OF SPIE

Imaging buried magnetic domains using hard x rays

Lang, Jonathan, Pollmann, J., Haskel, Daniel, Srajer, George, Maser, Jorg, et al.

SPIE.

Imaging buried magnetic domains using hard x-rays

J.C. Lang, J. Pollmann, D. Haskel, G. Srajer, and J. Maser
Advanced Photon Source, Argonne National Laboratory, Argonne,IL 60439

J.S.Jiang and S.D.Bader
Materials Science Division, Argonne National Laboratory, Argonne,IL 60439

ABSTRACT

Images of magnetic structures in a SmCo/Fe bilayer have been obtained using a circularly polarized hard x-ray microprobe. This probe combines circularly polarizing and microfocusing optics (either Fresnel zone plate or Kirkpatrick-Baez mirrors) to provide a highly polarized, small cross-section x-ray beam in the energy range between 5 and 12 keV. By using x-rays in this energy range, we can penetrate the top layers of the sample and therefore are able to measure the magnetic domains of buried magnetic structures with a resolution of ~5 µm. Contrast between magnetic domains is obtained by measuring the x-ray magnetic circular dichroism signal for different points as the beam is scanned across the sample. Images of the magnetic domain structure in a 1600-Å-thick buried SmCo layer of a SmCo/Fe bilayer were taken as a function of the externally applied magnetic field. These images show the nucleation of large domains ($\gtrsim$ 100 µm) whose domain walls are oriented perpendicular to the applied field direction. Upon increasing the applied field, the images show the growth of the local reversed domains as the domain walls propagate across the sample, leading to a complete reorientation of the hard magnetic layer.

Keywords: imaging, magnetism, x-ray optics, synchrotron radiation

1. INTRODUCTION

Since the microscopic magnetic domain structure plays a dominate role in controlling many of the macroscopic magnetic properties, such as the coercivity, understanding this structure is essential to a complete understanding of the magnetism in a material. Due to their technological applications, much research in magnetic materials has recently centered on multicomponent layered systems.[1] Obtaining magnetic structural information from such materials, however, posses some unique challenges. This is because established methods for imaging magnetic domains like scanning electron microscopy with polarization analysis (SEMPA), photoemission electron microscopy (PEEM),[2] or magneto-optical imaging, typically sample only the topmost portion of the sample ($\lesssim$20 nm), and therefore the measured magnetic structure is dominated by the surface.[3] Other domain imaging techniques, such as magnetic force microscopy (MFM) or soft x-ray (< 1 keV) magnetic dichroism imaging techniques,[4] like a magnetic transmission x-ray microscope (MTXM),[5] probe deeper than the above methods but are also limited in their penetrating power ($\lesssim$ 100 nm). Thus the magnetic structure of the layers beneath other magnetic or nonmagnetic capping layers is inaccessible via these techniques. Furthermore, imaging techniques that use emitted electrons, such as SEMPA and PEEM, typically can not be used with applied magnetic fields, hence studies of domain structures upon magnetization reversal could not be studied directly using these methods.

In this paper, we show that using a circularly polarized hard x-ray microprobe,[6] removes some of the limitations of the more conventional techniques. By using x-rays in the 5 to 12 keV range, we can penetrate the top layers of the structure and thus are able to measure the magnetic domain structure of the buried layers while an external field is applied. Furthermore, since the x-ray magnetic circular dichroism (XMCD) signal used to obtain contrast between domains involves a core-level resonance, a particular constituent in the material can be isolated, so that the resultant magnetic structural information is specific to a particular element in the compound. Lastly, the increased penetration

provided by the higher energy x-rays greatly relaxes the quality of surface required for measurements, therefore no special sample preparation is needed.

We have used this microprobe to study the magnetic domain structure of a SmCo layer in a SmCo/Fe bilayer. Composites of soft (Fe) and hard (SmCo) magnetic materials have shown a great deal of promise as new high strength permanent magnets.[7] In these composites, the soft magnet provides a high magnetic saturation, whereas the magnetically hard material provides a high coercive field.[8] Bilayers can be used as model systems to investigate the magnetization-reversal process in these composites,[9] where the hard magnetic material is grown epitaxially on a substrate to provide a well-defined magnetization axis, and the soft material is overlaid on top of it. When an external field is applied opposite to the magnetization direction of the bilayer, the soft layer will be pinned at the hard/soft interface but will twist along its thickness (as a spring). Upon removal of the external field, the soft phase will untwist and return to its previous alignment relative to the hard phase, thus leading to the name "spring magnet" or "exchange spring."[10]

Studies of the spatial magnetic structure in such bilayers, however, have been limited to measurements of the domains in the top soft layer. These studies have provided evidence for a biquadratic exchange coupling between the layers in this material. In this model, the bilayer behaves as described above for fields well below where the hard SmCo layer reverses magnetization, but as the applied field nears the SmCo reorientation, the soft Fe layer no longer springs back but rather remains locked at some angle with respect to the magnetization of the SmCo layer even after the applied field is removed. This non-colinear alignment of the hard/soft layer magnetizations is believed to arise from the formation of small domains in the SmCo layer. The Fe directly above an area, which has several SmCo domains, is in a frustrated state where the oppositely oriented domains try to magnetize the Fe in opposite directions. The Fe then chooses the lowest energy state by magnetizing at an angle with respect to both domains. This model has been developed solely by observing the magnetization of the soft layer only. By using our polarized x-ray microbeam, we are able to provide the first direct measurements of the magnetic structure in the buried SmCo hard layer.
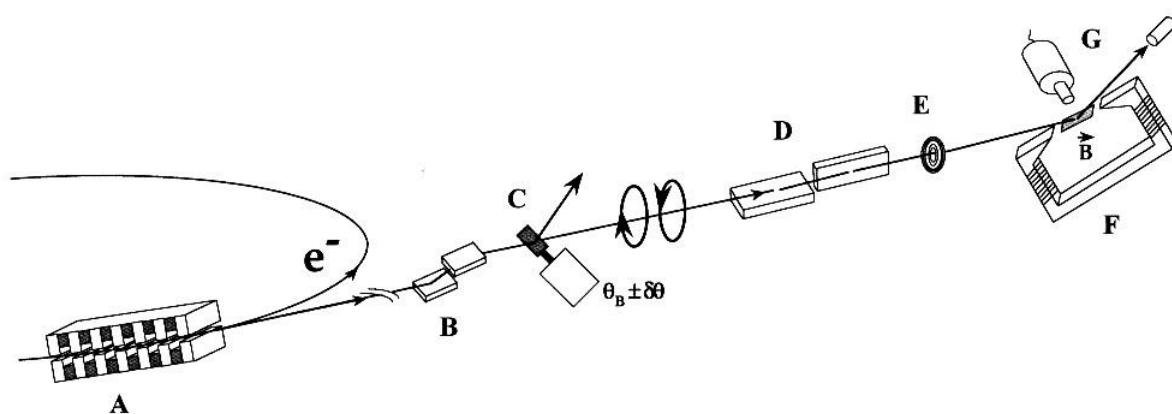

Figure 1: Schematic of the experimental setup. The x-ray beam from the undulator (A) is monochromatized by a Si (111) double-crystal monochromator (B). The linearly polarized x-ray beam is then converted to a circularly polarized beam using a diamond (111) transmission phase retarder (C). Either Kirkpatrick-Baez mirrors (D) or Fresnel zone plates (E) are subsequently used to focus the beam. The beam is then incident on the sample, which is placed between the poles of a 8.0 kG electromagnet (F). Detectors (G) can be used to monitor either the fluorescence or the diffracted beam.

2. EXPERIMENT

The experiment was performed at the SRI-CAT 4-ID-D insertion device beamline at the Advanced Photon Source (APS). A schematic of the experimental setup is shown in figure 1. The 4-ID-D beamline uses a standard planer APS undulator A.[11] This is a 3.3-cm-period insertion device with 70 periods capable of producing a highly linearly

polarized x-ray beam from 3.0 keV to energies greater than 100 keV. The beam is monochromatized using a cryogenically cooled Si (111) double-crystal monochromator, which provided an energy resolution of $\Delta E/E \approx 1.4 \times 10^{-4}$ in the 5 to 12 keV energy range. The polarized x-ray microbeam setup consists of two distinct optical components. First phase-retarding optics are used to convert the linearly polarized beam from the undulator into a circularly polarized one, and second a focusing setup is used to produce a micron sized beam. Either Fresnel zone plates (ZP) or a set of Kirkpatrick-Baez (KB) mirrors could be used for focusing the beam, depending on the experimental requirements. The beam was then incident on the sample, which was placed between the poles of an 8 kG electromagnet. A Ge solid-state detector was placed near the sample to measure the fluorescence x-ray magnetic circular dichroism signal. Alternately, the magnet and sample could be mounted on a diffractometer to measure the scattering analog to the XMCD signal (x-ray resonant exchange scattering, XRES).

2.1. X-ray magnetic circular dichroism

X-ray magnetic circular dichroism (XMCD) is used to provide a contrast mechanism sensitive to the relative orientation of the local magnetic moments.[12,13] XMCD measures the dependence of the x-ray absorption cross section (σ) on the degree of circular polarization in the incident photon beam (P_c) and the magnetization of the sample (M). For a relative angle θ between the helicity of the photon and the orientation of the magnetic moment of the absorbing atom, the x-ray absorption cross section takes the form,

$$\sigma = \sigma_{charge} + \sigma_{mag}; \quad \sigma_{mag} \; \alpha \; M \, P_c \cos\theta \,, \tag{1}$$

where σ_{charge} is the normal absorption that does not depend on the sample magnetization or helicity. By measuring the absorption cross section for opposite helicities ($\pm P_c$), the magnetic portion of the cross section (σ_{mag}) can be isolated. The local magnetization direction can then be deduced by taking the normalized difference {$(I^+ - I^-)/(I^+ + I^-)$ } or "flipping ratio." Furthermore, the XMCD effect only becomes appreciable near absorption edges. Since these absorption edges involve core-level electronic transitions, the measured spectra are specific to a particular element in the material. In the 5 to 12 keV range of this microprobe, difference signals of ~1% are observed for rare earth L edges and ~0.1% for transition metal K edges. For thin samples or those on x-ray opaque substrates (both the case for the SmCo/Fe sample), the transmitted signal is weak or lacks sufficient contrast, therefore the fluorescence yield from the sample can be used as a measure of the absorption. The fluorescence from the sample is proportional to the x-ray absorption and therefore is also sensitive to the XMCD signal.[14]

2.2. Phase retarding optics

Performing XMCD measurements requires a source of circularly polarized radiation. Synchrotron radiation, however, is naturally linearly polarized in the plane of the particle orbit. Several approaches for producing circularly polarized x-ray beams have been developed, based on either specialized insertion devices[15] or various types of crystal optics.[16] Between 5 and 12 keV, crystal optics based on transmission phase retarders have proven to be the most practical.[17] In this optic, a thin crystal is oriented near a Bragg reflection and the x-ray beam transmitted through the crystal used for the experiment. According to dynamical diffraction theory, the wave fields inside a crystal for different linear directions of polarization propagate with different phase velocities. The phase difference between these wave fields, δ, for a crystal of thickness, t, is a function of the deviation $\Delta\theta$ of the angle of incidence from the exact Bragg condition (θ_B),[18]

$$\delta = \frac{\pi}{2}\left(\frac{r_e \lambda^2}{\pi V}\right)^2 \frac{t}{\lambda} \frac{\sin(2\theta_B)}{\Delta\theta} \frac{}{\sin(\theta_B)} \mathrm{Re}\big[F_H F_{\bar{H}}\big]. \tag{2}$$

Here, r_e (2.818×10^{-5} Å) is the classical electron radius, λ is the x-ray wavelength, and F_H is the structure factor of the reflection. This phase difference is related to the degree of circular polarization in the transmitted beam by,

$$P_c = \frac{2\sqrt{I_\perp I_\parallel}}{I_\perp + I_\parallel} \sin\delta \quad , \qquad\qquad (3)$$

where $I_\parallel$ and $I_\perp$ are the intensities of the polarization components in and out of the scattering plane. To get a circularly polarized beam, these intensities must be the same, and the phase difference δ must be equal to $\pi/2$. Equal intensities can be obtained by inclining the diffraction plane of the phase retarder at 45˚ with respect to linear polarization of the incoming beam (horizontal), while the proper phase difference can be achieved for any thickness, t, or wavelength, λ, by adjusting the deviation $\Delta\theta$. Inverting $\Delta\theta$ by moving to either side of the Bragg reflection leads to an inversion of the helicity of circular polarization of the transmitted beam. Typically this rotation is of the order of tens of arcseconds. Therefore switching the beam helicity requires only minimal time and can be done several times during the course of a measurement, thereby reducing systematic errors. Crystals composed of low Z materials, such as diamond, produce the best phase retarders, since they balance the need to minimize the absorption in the transmitted beam while still producing reasonable deviations, $\Delta\theta$.[19]

For this experiment a 400-μm-thick diamond (111) crystal with 7x5 mm lateral dimensions was used for the phase retarder. The proper deviation, $\Delta\theta$, to obtain a circularly polarized beam for this phase retarder can be calculated using equation 2. Inserting the crystal thickness and the structure factor for the (111) reflection ($F_H = 12.27-i12.15$) yields a value of $\Delta\theta \approx 0.03$˚ for the 6.710 keV energy used in the experiment. Considering the divergence and energy spread in the incident beam, a circular polarization greater than 98% can be expected for either the right- or left-helicity transmitted beams.

2.3. Focusing optics

Two different optical setups were used to focus the beam; Fresnel zone plates (ZP)[20] and Kirkpatrick-Baez (KB)[21] mirrors. The ZP focusing setup provided a smaller focus size, and therefore better resolution, but the angular acceptance was small, so the overall flux on the sample was limited. The KB setup, on the other hand, increased the overall acceptance, thereby providing a much larger photon flux, but sacrificed some of the resolution due to a larger focal spot. Another difference between the ZP and KB optics is that the ZP setup focused the beam along the optical axis, thus measurements with the focused and unfocused beam could be taken without moving the sample/magnet, while with the KB setup deflected the beam both vertically and horizontally.

Zone plate optics are a well-established tool to produce x-ray beams with submicron crosssection. They can be understood as circular diffractive gratings with radially increasing line density, which focus the beam according to the Fresnel theory of diffracting zones.[22] The focal length f_m for the m-th order of diffraction of a ZP depends solely on the radius of the innermost zone r_1 and the wavelength of the radiation λ,

$$f_m = \frac{r_1}{m\lambda} \cdot \qquad\qquad (4)$$

For this experiment, a Au-based ZP with a thickness of 1.5 μm and a diameter of 250 μm was used. It was produced by combined electron-beam and x-ray lithography techniques.[23] At 6.71 keV the focal length of the ZP was ~33 cm. The ZP was mounted on a three-axis motorized stage to allow for linear alignment relative to the sample. Pinholes of various sizes, ranging from 20 to 50 μm, were used as order-sorting apertures (OSA), which block the higher diffraction orders produced by the ZP from striking the sample. The OSA was motorized for alignment in the x- and y-directions with a manual z-position (in-beam direction) adjustment. The beam size at the focus was measured using a Cr-coated knife-edge, which was scanned through the focus while monitoring the Cr K_α fluorescence, and found to be 3 x 5 μm^2 (vertical x horizontal) , with ~10^8 photons/s in the focal spot. This size is consistent the expected value from demagnification of APS particle beam source size ($\sigma_x = 359$ μm, $\sigma_y = 21$ μm).

The KB focusing setup consists of two mirrors, one reflecting vertically and the other horizontally. Each mirror is bent meridionally to provide separate focusing in the vertical and horizontal, respectively. The KB focusing optics used for this experiment are based on a design developed by the GeoCARS sector at the APS.[24] The mirrors were made

4   Proc. SPIE Vol. 4499

of single-crystal Si coated with Pt. Each mirror was ~100 mm long with a trapazoid shape (~50 mm one end down to ~20 mm on the other). Using the same method to measure the spot size as for the ZP setup, we measured a focal spot of 9 x 22 μm^2, with a photon flux of ~10^{10} photons/s. This spot was larger than expected, considering the focal distance ~40 cm was nearly the same as that for the ZP setup. The mirror substrates used, however, were known to have large surface figure errors which are thought to have degraded the focal size. We are currently in the process of procuring improved mirrors for this system, which should reduce the focus down to a size comparable to that obtained with the ZP setup.

2.4. Sample

The sample studied was a 200 Å Fe/1600 Å SmCo/200 Å Fe/200 Å Ag layer grown epitaxially on a 1-mm-thick MgO (110) substrate using dc magnetron sputtering. The SmCo was nominally deposited in the Sm_2Co_7 phase, although there are local deviations from the ideal stoichiometry, leading to regions with $SmCo_5$ or $SmCo_3$ phases.[25] The c-axis of the SmCo film, which is the easy magnetization direction, grew in the plane of the sample. By adjusting the growth conditions, the orientation of the c-axis within the plane of the sample could be aligned, such that the sample had uniaxial magnetic anisotropy. The in-plane alignment of the c-axis was confirmed by measuring the easy-axis magnetization loops using SQUID magnetometry.

2.5. Data collection

Measurements were performed at the Sm L_3 edge, by monitoring the L_α fluorescence intensity. To determine the energy that provided the best magnetic contrast, XMCD spectra were first taken as a function of energy with an unfocused beam and the sample fully aligned (see figure 2). From figure 2, the largest difference clearly occurs near 6.710 keV (6 eV below the absorption edge). This energy was subsequently used for all the measurements of the magnetic domain images. Magnetic domain images were recorded as a function of the externally applied magnetic field. The sample was scanned in two dimensions through the microfocused beam, using Newport MFN series stages (0.1 μm resolution). A magnetic field of up to 8 kG was applied parallel to the axis of easy magnetization. The helicity of the beam was reversed at each data point, and the flipping ratio was used as a measure of the local magnetization.
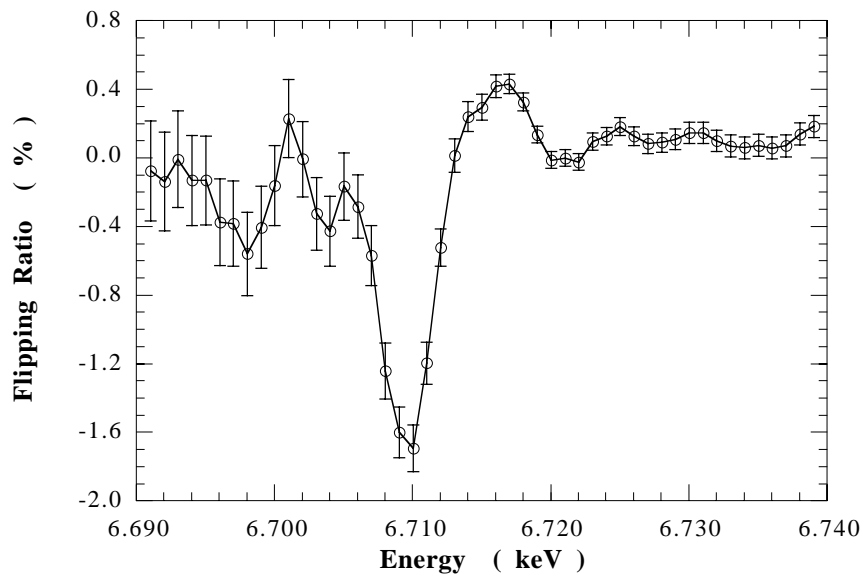

Figure 2: XMCD spectra as a function of energy showing the optimum contrast at 6.710 keV.

3. RESULTS

Figure 3 shows a series of magnetic domain images of the SmCo layer, taken with the ZP (left) and with the KB (right) focusing setups for different applied magnetic fields. The field was applied in the plane of the sample along the easy magnetization axis. The sample and magnetic field were oriented 45˚ to the x-ray beam direction. This angle provided a good trade off between having the magnetization parallel to the beam, which maximizes the XMCD signal (see equation 1), and smearing of the focal spot due to the footprint of the x-ray beam on the sample. The relative position of each image along the sample magnetization curve, measured using SQUID magnetometry, is also indicated. The colors in the images correspond to the measured flipping ratios given by the scale on the right. A red color denotes a region where the local magnetization is antiparallel to the incoming beam, and a blue color is where it is parallel.

The first set of images obtained, shown on the left side of figure 3, were taken using the ZP focusing setup. These images measure an area of 50x50 µm^2 in 2 µm steps. Data collection for each image took approximately ~3 to 4 hrs for this setup. From the position of the ZP images on the magnetization curve, it is clear that the reversal of the magnetization in the sampled area occurs over a much narrower field range than that of the entire sample (see discussion below). Therefore a second set of images was taken using the KB setup. These images, shown on the right side of figure 2, measure an area of 250x500 µm^2 (vertical x horizontal) in 10 and 20 µm steps, respectively. Thus the KB images cover an area 50 times greater than those measured using the ZP setup. Data collection for each KB image took ~1hr. The data collection time was greatly reduced for with the KB setup since the incoming photon flux was much larger. The images taken with either the ZP and KB setups take a considerable amount of time to acquire since measuring differences of ~1%, requires the accumulation of considerably more counts than a standard fluorescence mapping measurement.
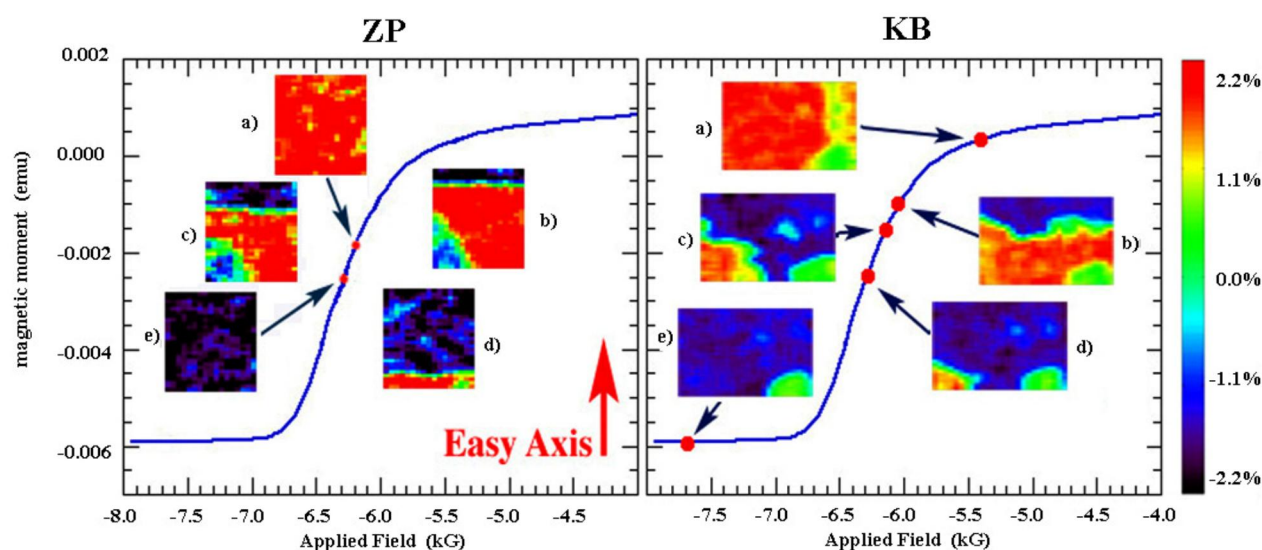

Figure 3: Images of the magnetic structure of the buried SmCo layer as a function of the applied field taken using the ZP (left) and KB (right) focusing optics. The field was applied along the easy axis, which is the vertical direction in both sets of images. The ZP images cover a sample area of 50x50µm^2 and were taken with applied fields of -6.22 kG (a), -6.24 kG (b), -6.28 kG (c), -6.32 kG (d), and -6.42 kG (e). The KB images cover an area of 250x500 µm^2 and were taken at fields of -5.40 kG (a), -6.04 kG (b), -6.17 kG (c), -6.27 kG (d), and -7.70 kG. The colors on the images correspond to the measured flipping ratios, red indicates a domain where the net local magnetization is antiparallel to the incident beam direction and blue indicates a region where it is parallel. The blue line corresponds to the macroscopic hysterisis of the sample measured by SQUID magnetometry.

4. DISSCUSSION

Both the ZP and KB images shown in figure 3 clearly show domains with different orientations of the local magnetic moments. The reversal of these magnetic domains in the SmCo layer upon increasing applied field is also resolved, showing the growth of separate domains at the expense of the oppositely oriented intermediary domains. Several qualitative statements can be made about this process; i) the reorientation of the magnetization in the images occurs over a smaller applied field range than that measured for the entire sample, ii) the domains that nucleate are large, and iii) boundaries between these domains are oriented perpendicular to the easy axis of magnetization (and the applied field).

The range over which the microscopic reorientation occurs for the ZP images (<100 G), is quite small compared to the one in the macroscopic hysteresis curve measured with the SQUID magnetometer. This leads to the conclusion that the observed hard layer reorientation is localized and other sections of the sample have different nucleation fields. The breadth of the hard layer reversal measured by magnetometry is therefore probably due to the this distribution of nucleation fields. This is supported by the KB image measurements, since the much large area measured in these images increased the observed reorientation field substantially (>300 G).

The size of the domains is quite surprising, especially for KB images where the domain wall extends across the entire 500 μm width (see image (b) in figure3). From previous measurements of the domains in the Fe layer of these systems,[10] many nucleation centers were expected across the field of view of KB images. These previous measurements, however, were taken on a bilayer with a 200-Å-thick SmCo layer in remanence, while our measurement was performed on a sample with a 1600-Å-thick layer under an applied field. This difference in thickness and field conditions could possibly change the microscopic magnetic properties enough to account for the observed difference. Further measurements on thinner samples are planned to explore this.
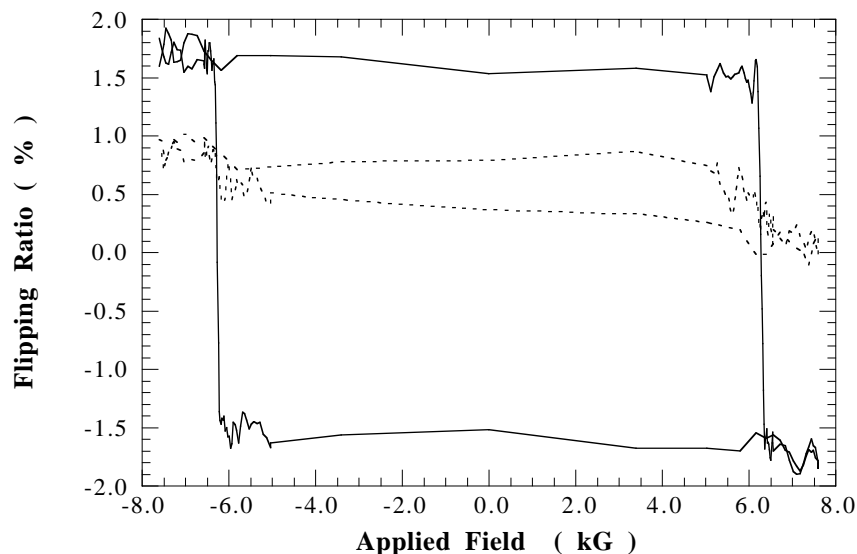

Figure 4: Localized magnetic hysteresis measurements in the high contrast (solid) and low contrast regions (dotted) of the KB images.

The direction of the domain walls can be understood from the chemical structure of the SmCo layer. The axis of easy magnetization in SmCo films is given by the c-axis of the Sm_2Co_7 unit cell.[26] Stacking disorders induced by the $SmCo_5$ or $SmCo_3$ phases mentioned earlier will be oriented perpendicular to the easy axis. These stacking disorders effectively pin the domain walls. Deviations from this preferred orientation of domain walls seen in the lower left corner of the ZP images and the lower middle portion of the KB images in figure 3 may be due to other structural defects. This

assumption is supported by the fact that the sum of the fluorescence signals in the ZP images, corresponding to the Sm concentration, shows variations on the order of 10% of the average signal, which are strongly correlated to the observed magnetic structures.

Another interesting feature is found at the lower right portion of each of the KB images (green area). In this region very little magnetic contrast was observed for any applied fields. To investigate this further we performed local hysteresis measurements (shown in figure 4) at the center of this region and at a point where we observed clear domain formation. Figure 4 shows that, although the contrast is much smaller than that from the other parts of the sample, there is some change in the magnetization in this region also. We believe that the much smaller signal is due to either a local Co deficiency in this region or a misorientation of the epitaxial growth resulting in a crystal grain whose easy axis is oriented nearly perpendicular to the x-ray beam.

In conclusion, we were able to determine for the first time the orientation of magnetic domains in a SmCo layer buried beneath another ferromagnetic layer of Fe. Large domains were observed to nucleate in the Sm Co layer with domain walls oriented perpendicular to and propogating along the applied field direction. The range of field required to reverse the magnetization of the sample on the microscopic level was much less than for the macroscopic measurements. This was believed to arise from a distribution of domain nucleation fields across the sample.

REFERENCES

1. G.A. Prinz, *Phys. Today* **48**, 58 (1995).
2. J. Stöhr, Y. Wu, B.D. Hermsmeier, M.G. Samant, G.R. Harp, S. Koranda, O. Dunham, and B.P. Tonner, *Science* **259**, 658 (1993).
3. R.J. Celotta, J. Unguris, M.H. Kelley, and D.T. Pierce, "Techniques to measure magnetic domain structures" in *Methods in Materials Research: Current Protocols*, edited by E. Kaufmann, Ch. 6b.3 (John Wiley & Sons, New York, 2000).
4. J. Stöhr, H.A. Padmore, S. Anders, T. Stammler, and M.R. Scheinfein, *Surf. Rev. Lett.* **5**, 1297 (1998).
5. P. Fischer, T. Eimüller, G. Schütz, G. Denbeaux, A. Pearson, L. Johnson, D. Attwood, S. Tsunashima, M. Kumazawa, N. Takagi, M. Köhler, and G. Bayreuther, *Rev. Sci. Instrum.* **72**, 2322 (2001).
6. J. Pollmann, G. Srajer, J. Maser, J. C. Lang, C. S. Nelson, C. T. Venkataraman, and E. D. Isaacs, *Rev. Sci. Instrum.* **71**, 2386 (2000).
7. J.S. Jiang, E.F. Fullerton, C.H. Sowers, A. Inomata, S.D. Bader, A.J. Shapiro, R.D. Shull, V.S. Gornakov, and V.I. Nikitenko, *IEEE Trans. Mag.* **35**, 3229 (1999).
8. E.F. Kneller and R. Hawig, *IEEE Trans. Mag.* **27**, 3588 (1991).
9. E. F. Fullerton, J. S. Jiang, M. Grimsditch, C. H. Sowers, and S. D. Bader, *Phys. Rev. B* **58**, 12193 (1998).
10. V.K. Vlasko-Vlasov, U. Welp, J.S. Jiang, D.J. Miller, G.W. Crabtree, and S.D. Bader, *Phys. Rev. Lett.* **86**, 4386 (2001).
11. R.J. Dejus, B. Lai, L.R. Moog, and E. Gluskin, Argonne National Laboratory Report No. ANL/APS/TB-17 (1993).
12. G. Schütz, W. Wagner, W. Wilhelm, P. Kienle, R. Zeller, R. Frahm, and G. Materlik, *Phys. Rev. Lett.* **58**, 737 (1987).
13. J.C. Lang, "X-ray magnetic circular dichroism" in *Methods in Materials Research: Current Protocols*, edited by E. Kaufmann, Ch. 10c.2 (John Wiley & Sons, New York, 2000).
14. P. Strange, P.J. Durham, and B.L. Gyorffy, *Phys. Rev. Lett.* **67**, 3590 (1991).
15. A. Agui, A. Yoshigoe, et al., *Rev. Sci. Instrum.* **72**, 3191 (2001).
16. K. Hirano, T. Ishikawa, and S. Kikuta, *Nucl. Instrum. Methods* **A336**, 343 (1993).
17. J.C. Lang, G. Srajer, and R.J. Dejus, *Rev. Sci. Instrum.* **67**, 62 (1996).

18. J. C. Lang and G. Srajer, *Rev. Sci. Instrum.* **66**, 1540 (1995).
19. C. Giles, C. Malgrange, J. Goulon, C. Vettier, F. de Bergevin, A. Freund, P. Elleaume, *Proc. SPIE* **2010**, 136 (1993).
20. G. Schmahl and P.-C. Cheng, " X-ray microscopy" in *Handbook on Synchrotron Radiation* edited by S. Ebashi, M. Koch, and E. Rubenstein, Vol. 4, Ch. 15 (Elsevier Science, New York, 1991).
21. P. Kirkpatrick and A.V. Baez, *J. Opt. Soc. Am.* **38**, 766 (1948).
22. M. Born and E. Wolf, *Principles of Optics* (Cambridge University Press, Cambridge, 1980)
23. W. Yun, B. Lai, Z. Cai, J. Maser, D. Legnini, E. Gluskin, Z. Chen, A.A. Krasnoperova, Y. Vladimirsky, F. Cerrina, E. Di Fabrizio, and M. Gentili, *Rev. Sci. Instrum.* **70**, 2238 (1999).
24. P.J. Eng, M.L. Rivers, B.X. Yang, W. Schildkamp, *Proc. SPIE* **2516**, 41 (1995).
25. M. Benaissa, K.M. Krishnan, E.F. Fullerton, and J.S. Jiang, *IEEE Trans. Mag.* **34**, 1204 (1998).
26. E. F. Fullerton, J. S. Jiang, C. Rehm, C. H. Sowers, S. D. Bader, J. B. Patel, and X. Z. Wu, *Appl. Phys. Lett.* **71**, 1579 (1997).